Numerical Evaluation of Pin-Bearing Strength for the Design of Bolted Connections of Pultruded FRP material

Ana M. Girão Coelho

Lecturer (former Marie Curie IEF Research Fellow at the University of Warwick)

(ana.girao-coelho@ncl.ac.uk)

School of Engineering and Geosciences, Newcastle University, Newcastle upon Tyne, UK

J. Toby Mottram

Professor

(corresponding author: j.t.mottram@warwick.ac.uk)

School of Engineering, University of Warwick, Coventry, UK

orcid.org/0000-0002-2750-8125

Abstract: Presented in this paper are finite element (Abaqus) predictions for the strength of a pultruded fibre reinforced polymer material subjected to pin-bearing loading with hole clearance. One of the distinct modes of failure in steel bolted connections is bearing. It is caused by the compression action from the shaft pressing into the laminate, and when there is no lateral restraint the mechanism observed at maximum load shows 'brooming' for delamination failure.

Each lamina in the glass fibre polyester matrix material is modelled as a homogeneous, anisotropic continuum and a relative very thin resin layer is assumed to contain any delamination cracking between stacked layers. A cohesive zone model is implemented to predict the size and location of the initial delamination, as well as the load-carrying capacity in a pin-bearing specimen. Finite element simulations (as virtual tests) are performed at the mesoscale level to validate the modelling methodology against experimental strength test results with delamination failure, and to show how pin-bearing strength varies with parameter changes. For an example of the knowledge to be gained for the design of bolted connections, the parameteric study where the mat reinforcement is either continuous strand or triaxial (+45º/90º/-45º/chopped strand) shows the latter does not provide an increase in pin-bearing strength.

Introduction

Shapes made by the pultrusion composite processing method consist of thin-walled laminated panels of glass Fibre Reinforced Polymer (FRP) matrix connected to form open or closed cross-sections. Because I, wide flange, channel, box and leg-angle shapes mimic steel sections it is natural that frame construction follows what is seen in conventional steelwork (Creative Pultrusions 2016; Strongwell 2016; Turvey 2000). Being lightweight and resistant to corrosion, and having expected low life cycle costing, pultruded structures are increasingly used where these attributes meet the requirements of the construction project, such as for pedestrian bridges (Anonymous 2016).

Introduced in Mottram and Zafari (2011) is the rationale for steel bolting to be a main method of connection (Creative Pultrusions 2016; Strongwell 2016), and the requirement that, for strength design, a reliable test method is needed to determine bearing strengths. The *bearing strength* is an important material parameter for static strength design (Bank 2006; Mottram and Turvey 2003), and can be characterized as the resistance of the material to a fastener loaded hole. Strength depends on a number of parameters including: FRP thickness (t); FRP mechanical properties; FRP material orientation to the bearing force; bolt material; bolt diameter (d); clearance hole size. In bolted lap-joints the end distance (e_1), which is the distance from the centre of the hole to the free edge perpendicular to the loading direction has to exceed a limiting value for the bearing failure mode to govern.

An advantage for bolted connection design failing in the bearing mode is that it might provide the connection/joint with a degree of damage tolerance and structural integrity. Bearing failure can be enhanced by: (i) correctly sizing the connection, usually end distance to fastener diameter ratio $e_1/d \geq 3$ providing the width to fastener ratio is 4 or higher, see Bank (2006), and Girão Coelho and Mottram (2015a); (ii) the choice of the fibre reinforcements in the lamination stacking sequence.

Mottram and Zafari (2011) justify why the measurement of bearing strength for design calculations must be for the lower bound pin-bearing value. The pin-bearing condition assumes the

61   steel bolt shaft has no thread in bearing and that there is no lateral restraint, which will not initially

62   exist in practice because the washer, nut, bolt combination should be tightened. The paper explains

63   the reasons for having a strength test method for pin-bearing strength with a plate-shaped coupon

64   that is no larger in size than, say 80×80×t mm. Using an in-house test approach, detailed in Mottram

65   and Zafari (2011) or Matharu (2014), numerous test results have been reported from programmes of

66   characterization work (see also Zafari and Mottram 2012) to understand the variations in pin-

67   bearing strength and characteristic values for pultruded materials. Two different materials were

68   studied, and in the test matrix parameters were: four bolt diameters, e.g. 9.53 mm (3/8 in.), 12.7 mm

69   (1/2 in.), 15.8 (5/8 in.) and 25.4 mm (1 in.) (Mottram and Zafari 2011) or M10, M12, M16 and M20

70   (Matharu 2014); different material orientations (e.g. 0°, 90° and 45°); non-aged and hot-wet aged

71   materials. One aim of the characterization work was to obtain data on how pin-bearing strengths

72   might change in the field due to the long-term effect of exposure to a site's environment.

73   Both materials were from the American pultruder Creative Pultrusions (2016) having glass

74   fibre reinforcement in the form of alternative layers of unidirectional rovings and a mat, and a fire-

75   retardant matrix of an isophthalic polyester polymer. For the Mottram Zafari (2011) and Zafari and

76   Mottram (2012) tests the pultruded material was from the standard 1525 series having mat

77   reinforcement of a Continuous Strand Mat (CSM) having a random arrangement of continuous

78   fibres. Matharu's (2014) work was with material from the Pultex® SuperStructural 1525 series, and

79   the main difference is that the mat reinforcement is triaxial, having unidirectional fibres at 90°, and

80   ±45° and a 'thick' backing of a chopped strand fibres. Another difference in the test matrix with

81   Matharu is that testing was with and without bolt thread in bearing; only the latter connection

82   condition can be linked to the Finite Element (FE) work presented in this paper.

83   The FE modelling methodology applied by the authors uses options solely available from the

84   general purpose software Abaqus with its implicit solver (2016). Girão Coelho *et al*. (2016)

85   introduce, and show how the approach is modelling the various failure modes, and, in particular, for

86   the parametric studies given later the critical mode of progressive delamination using cohesive zone

87 models. A similar approach using Abaqus/Explicit has been reported by Du *et al*. (2016) with their

88 progressive damage analysis implemented via a user subroutine VUMAT. Because no customized

89 user-subroutines are required with the author's modelling methodology the computational results

90 using Abaqus implicit can be universally reproduced. Simulation outputs for pin-bearing strengths

91 will be validated using non-aged test results from Matharu (2014), and in a strength comparison

92 using data from Mottram and Zafari (2011) for changing the mat reinforcement. The main

93 contribution of this paper is the predictions from a series of parametric studies to investigate how

94 pin-bearing strength might vary with changes in the fibre reinforcement.

95

96

97 ## Fundamental Behaviour and Analysis Approach

98

99 Bearing failure is a mode showing local crushing and delamination of the laminated material in

100 direct contact with the steel bolt shaft (Bank 2006; Mottram and Turvey 2003). The bearing strength

101 of monolithic materials (e.g. steel) is generally evaluated without lateral restraint or through

102 thickness constraint from a bolt tightening. Application of this test condition with FRP composites

103 allows delamination fracturing to occur. In this paper the word *delamination* has the meaning for the

104 formation and growth of a flat flaw in an initially flawless interface (between two previously

105 'bonded' laminae) that grows into a sizeable delamination crack. With PFRP materials this failure

106 mechanism leads to the lowest bearing strength.

107 The presence of composite material viscoelasticity (Mottram 2005), and the influence of

108 structural actions on the bolted connection ensure that it will be unreliable to assume there can

109 always be lateral restraint at the end of the design working life, which can for a structure be, 50 or

110 100 years. It is for this reason (Mottram and Zafari 2011) that the *pin-bearing strength* has to be the

111 strength used in design calculations for bolted connection strength design.

112   The FE study presented next to model the bearing behaviour includes a *continuum damage*

113   *model* with a *cohesive zone approach*. Continuum damage models address the *intralaminar failure*

114   *mechanisms* from a global standpoint, whereas if the analyst used individual damage mechanisms

115   they would be homogenized and constructed around a failure criterion (Knops 2008). This approach

116   is the least complex and uses the composite lay-up modeller tool within the Abaqus (2016) pre-

117   processor to define the individual laminae through a laminate thickness. Each layer is cohesively

118   bonded together to form the *lamination with interfaces* assumed to have a thickness of $10^{-3}t_{lay}$,

119   where t_{lay} is the thickness of the thinnest layer either side of the interface. Values for t_{lay} are

120   introduced in the section for the *Description of the Model*. This modelling dimension plays the role

121   of a length scale, and it has been shown by Girão Coelho (2016) that the thickness of the cohesive

122   interface does not affect the computational performance provided its thickness is small enough

123   compared to t_{lay}.

124

125

Modelling of Progressive Delamination Using Cohesive Zone Models

127

128   Delamination failure is the separation of reinforcing layers from each other, as a consequence

129   of shear stresses acting in planes parallel to the layers' interfaces and/or tensile stresses acting in the

130   through-thickness direction. This phenomenon is a typical *crack growth* problem and is treated in

131   the framework of fracture mechanics (Girão Coelho 2016). Today, the most popular computational

132   method for the prediction of delamination failure is based on *cohesive zone models* that provide a

133   natural bridge between strength-based models and energy-based models for fracture. This allows

134   delamination to be described by a single framework that covers a range of applications for which,

135   on their own, neither a strength nor an energy criterion might not be sufficient.

136   Cohesive zone models consider fracture as a gradual phenomenon in which separation takes

137   place across an extended crack tip, or cohesive zone, and is resisted by cohesive tractions (Ortiz and

138   Pandolfi 1999). Thus cohesive zone elements do not represent any physical material, but describe

139   the cohesive forces which occur when layers in the lamination are being pulled apart. In FE

140   modelling, cohesive zone elements are placed between the continuum elements used to model the

141   individual laminae. A key analysis feature of these elements is that they include the effect of first

142   delamination failure, and the subsequent crack propagation by means of critical strain energy

143   release rates.

144   In our modelling methodology, see Girão Coelho *et al*. (2016), the simulation of interlaminar

145   damage is based on the cohesive zone approach using the Abaqus three-dimensional cohesive

146   element COH3D8. The study is performed in the quasi-static regime. The traction-separation law

147   formulation assumes a non-zero elastic stiffness of the cohesive zone, which is physically motivated

148   by the reduced stiffness of the matrix-rich very thin interface layer (t_{lay}) as compared to a perfect

149   bond assumed to exist between the fibres and the surrounding polymer matrix. From a numerical

150   point of view, this elastic stiffness can be understood as a penalty-type enforcement of displacement

151   continuity in the elastic range.

152   A quadratic stress criterion is used for the *damage initiation criterion*. To specify the

153   conditions for separation in the cohesive zone model the following expression is chosen (Brewer

154   and Lagace 1988; Camanho *et al*. 2003):

155
$$\left(\frac{\langle\sigma_n\rangle}{f_I}\right)^2+\left(\frac{\sigma_s}{f_{II}}\right)^2+\left(\frac{\sigma_t}{f_{III}}\right)^2=1 \tag{1}$$

156   where σ_n is the stress in pure opening mode, σ_s is the stress in the first shear direction, σ_t is the

157   stress in the second shear direction, f_I (opening), f_{II} (sliding)) and f_{III} (tearing) are the peak strength

158   values in the same directions, and:

159
$$\langle\sigma_n\rangle=\sigma_n \quad \text{for} \quad \sigma_n>0 \qquad \text{and} \qquad \langle\sigma_n\rangle=0 \quad \text{for} \quad \sigma_n\leq0. \tag{2}$$

160   The latter modelling constraint in Eq. (2) is because compressive normal stresses cannot open a

161   delamination crack.

162   *Progression of damage at the interfaces* is modelled using a linear softening law and a critical

163   mixed mode energy behavior based on the Benzeggagh-Kenane criterion (1996), which is described

164   by the following expression:

165                         $$G_{\mathrm{c}} = G_{\mathrm{I,c}} + \left(G_{\mathrm{II,c}} - G_{\mathrm{I,c}}\right)\left[G_{\mathrm{II}}/\left(G_{\mathrm{I}} + G_{\mathrm{II}}\right)\right]^{\eta}.$$ (3)

166   In Eq. (3) $G_{\mathrm{m,c}}$ (with m = I, II, III) is for the total critical strain energy release rate associated

167   with delamination mode m, and η is for the semi-empirical criterion exponent applied to

168   delamination initiation and growth. Based on the argument given by Girão Coelho (2016) exponent

169   η is assumed to be 1.5. Illustrated in Figs. 1(a) to 1(c) are the three distinct opening modes that can

170   occur singularly or interact together to cause the initiation and formation of a delamination failure.

171   The use of cohesive zone models requires that a very fine mesh specification is used to ensure

172   that sufficient interface elements exist within the cohesive zone length where the crack tip is

173   moving. If the mesh design happens to be too coarse, the cohesive stress at the discontinuity may

174   not even reach the interfacial strength and, as a result, the required failure mode is missed. Falk *et*

175   *al*. (2001) suggest a minimum of two to five elements in this cohesive zone length in order to

176   perform a reliable simulation. Turon *et al*. (2000) indicate that for typical graphite-epoxy or glass-

177   epoxy FRP materials, the length of the cohesive zone should be smaller than one or two millimetres.

178   As a consequence, the mesh size required in order to have more than two elements in the cohesive

179   zone should be smaller than half a millimetre. For full-sized structural models of pultruded shapes

180   and structures this has the obvious consequence of a computationally expensive solution. Current

181   numerical simulations for the 80×80×9.5 mm pin-bearing specimen comply with the cohesive zone

182   element mesh size requirements specified by the first author (Girão Coelho 2016) to allow stable

183   numerical simulations of interface delamination.

184

185

186   **Finite Element Validation of Strength Behaviour**

187

188   A general FE model for the pin-bearing problem is developed and validated in this section using

189   experimental strength results from the PhD work by Matharu (2014). Note that the objective of the

190   FE work is to obtained predictions for the pin-bearing strength, which is established by the

191   maximum test load (or stress, which is this load divided by the projected bearing area given by pin

192   diameter times specimen thickness). There are engineering/scientific reasons why the FE

193   simulations might not be numerically reliable in predicting the onset of damage and all of the modes

194   of failure that occur prior to peak load. There is a likelihood that piror to loading there are already

195   matrix cracks (running parallel to the unidirectional fibre) because of residual thermal strain owing

196   to the cooling down from a temperature of 150°C in the pultrusion composite processing.What is

197   known from the extensive programme of static strength tests by Matharu (2014), and by Mottram

198   and Zafari (2011), is that when the bearing load is aligned in the direction of pultrusion the load-

199   stroke curve (testing machine displacement) is virtually linear elastic until to ultimate failure, which

200   always occurs with a noticeable load reduction and audible acoustic emissions. This signal of

201   ultimate failure is too pronounced to be for initial/new matrix cracking, and when the post-failure

202   load is released inspection of the bearing surface shows there to be interfacial delamination

203   fractures. This is the authors' evidence-based justification for how the FE invetigation was carried

204   out and reported in this paper.

205   Matharu (2014) tests are for pultruded material taken from the web of a Pultrex®

206   SuperStructural wide flange shape with nominal thickness of 9.53 mm (3/8 in.) (Creative

207   Pultrusions 2016); the measured thickness is closer to 9.6 mm. The test matrix has plain steel pins

208   of four metric diameters from 10 to 20 mm diameter with a clearance hole size that introduced the

209   maximum allowable fabrication tolerance using the guidance in Anonymous (2012) from the

210   Pultrusion Industry Council, USA. The technical reason for the maximum is that the bigger the hole

211   clearance is, the lower is the pin-bearing strength (Yuan 1996), and for a safe design the lowest

212   characteristic strength is required (Mottram and Zafari 2011). Without the fabrication tolerance the

213   recommended clearance size is 1.6 mm (or 1/16 in.) (Anonymous 2012; Creative Pultrusions 2106;

214 Strongwell 2012). The nominal clearance ($d_0 - d$) is 2.2 mm (given by 1.6 mm clearance +0.4 mm

215 tolerance) for M10 and 2.4 mm (1.6 mm clearance +0.8 mm tolerance) for M12, M16 and M20 bolt

216 sizes. After drilling a pilot hole of diameter less than required the final hole dimeter to ±0.02 mm

217 was prepared using a Cinccinati Arrow 450 Milling machine. Batches of ten nominally identical

218 specimens were tested to determine the pin-bearing strength that is statistically analysed and

219 critically evaluated by Matharu (2014).

220   The geometry was taken comparable to the experimental set-up, with the pin diameter as FE

221 modelling parameter. Fig. 2 defines the specimen geometry and shows the layered structure of the

222 SuperStructural web material.

223   Specific characteristics and attributes that were incorporated into the modelling are:

224 1. Based on the relatively high stiffness of the steel pin with respect to the longitudinal web

225   material, *c.f.* 210 kN/mm^2 (BS EN 1993-1-1:2005) to 21.3 kN/mm^2 (Creative Pultrusions

226   2016)), the bearing load is exerted by a rigid (circular smooth) pin, this is shown in Fig. 2.

227 2. Interaction between pin and hole is not only modelled with a normal bearing load, but also

228   with a through-thickness friction having a friction coefficient taken equal to 0.25, based on

229   the testing by Mottram (2005) to account for the FRP/steel contact.

230 3. Residual thermal stresses resulting from the pultrusion thermal-induced and cure-induced

231   shrinkage processes are not considered. Chen *et al*. (2001) and Zhang *et al*. (2004) developed

232   micro-mechanical models that have been successfully employed in computational analysis

233   and showed that initial residual stresses within pultruded structural shapes dissipate over time

234   owing to viscoelastic creep relaxation (Bank 2006).

235

236

237 ***Material Properties***

238   This section describes the physical and mechanical properties of the original material used in

239 the extensive testing programme by Matharu (2014). The pultruded material is from the Pultex$^{®}$

240 SuperStructural 1525 series of 'off-the-shelve' shapes. Identifier 1525 means the thermoset

241 polyester matrix is Class 1 Flame Retardant. The E-glass FRP fibre architecture consists of mat

242 layers interspersed with nominally constant thickness layers of UniDirectional (UD) rovings having

243 a fibre volume fraction of 60%. The mat reinforcement is type E-TTXM 4008, a Triaxial Stitched

244 Fabric Mat (TSFM) from Vectorply Corporation (http://vectorply.com/wp-

245 content/uploads/2015/06/E-TTXM-4008.pdf). The pultruded shape has an outer (relatively thin at

246 0.03 mm (see Table 1)) surface veil (non-structural) for UV protection and a barrier to moisture

247 diffusion. The NEXUS® veil layer is resin-rich, non-structural and consists of randomly orientated

248 short 100% melt polyester fibres, which has a mass per unit area < 100 g/m^2.

249   As seen in Fig. 2 there are five alternating layers of UD and TSFM, with two TSFM layers at

250 mid-thickness having no UD layer between them. TSFM is of a stitched continuous fabric having

251 four layers with the lay-up sequence of +45°/90°/–45°/random chopped strand. Assuming the

252 volume fraction of fibres in the continuous layers is 60% the chopped strand backing layer in TSFM

253 has a volume fraction of 16%. The thicknesses of the layers are 0.35 mm for the 90°, 0.51mm for

254 the ±45° and 0.54 mm for the chopped strand. It is known from Creative Pultrusions Inc. that the

255 UD layers comprise of 56 yield rovings.

256   The thermoset resin is the Reichhold 31031 unsaturated isophthalic polyester resin. To produce

257 a matrix for the pultrusion composite processing there are additives and fillers. The largest

258 proportions in the formulation, which consist of 13 constituent parts, is for the polyester resin, at

259 approximately 80% of the bulk matrix.

260   A series of resin burn-off tests were conducted by Matharu (2014) to estimate the volumetric

261 proportions of UD and TSFM fibres, and matrix, as well as to establish the nominal thicknesses of

262 each layer. The resin burn-off procedure was adapted from the method described in Appendix B of

263 the PhD thesis by Lane (2002), and with reference made to the testing procedure given in Ye *et al*.

264 (1995) and ASTM D2584-11 (2011). Table 1 summarizes the results from the resin burn-off tests.

265 Because the reinforcing effect of the Surface Veil (SV) layers is minimal it can be seen that the total

266 amount of glass fibre with the two main reinforcing laminae of UD and TSFM are equal at 34%

267 volume fraction. The volume percentages of UD, TSFM and matrix are in the range 30 to 34. The

268 final row in Table 1 reports the nominal thicknesses of the layers (the t_{lay}s) on the assumption that

269 they are constants for a particular reinforcement type in the original material. Note that both the veil

270 and TSFM thicknesses are predetermined by their construction. Only the UD layers have a freedom

271 to have a processing variation for layer thickness.

272   The mechanical properties presented in Table 2 are defined with respect to the local co-ordinate

273 system, with: 1 for the pultrusion direction; 2 for the in-plane direction normal to the direction of

274 pultrusion; 3 for the through-thickness direction. In the literature the direction of pultrusion is often

275 referred to as the longitudinal (or length-wise) direction and the perpendicular (in-plane) direction

276 as the transverse (cross-wise) direction. Notation f_1 is therefore for the in-plane longitudinal

277 strength, f_2 for the in-plane transverse strength, $f_{1,S}$ for the in-plane shear strength, and $f_{2,S}$ for the

278 transverse shear strength. Values in the table for Tensile (T) and Compressive (C) actions are for in-

279 plane strengths.

280   The determination of the elastic constants for the three different laminae are reported in Table 2

281 was carried out using micromechanical modelling with volume fractions of the constituents

282 established by using the resin burn-off method, as described in Lane (2002). In making the

283 micromechanical modelling calculations, it is assumed that the densities of matrix and glass fibres

284 are 1.1 g/cm^3 (Reichhold, 2006) and 2.56 g/cm^3 (Hancox and Mayer, 1994), respectively. The

285 modulus of elasticity for the matrix constituent is assumed to be 3.2 kN/mm^2 (Reichhold, 2006) and

286 for the fibres it is taken as 72 kN/mm^2 (Hancox and Mayer, 1994). The constituent Poisson's ratios

287 are assumed to be 0.36 and 0.22, respectively. Using the rule of mixtures approach with the two

288 lamina stiffnesses in Table 2 predictions for the elastic constants of the 9.6 mm thick panel are $E_1 =$

289 25.0 kN/mm^2, $E_2 = 16.7$ kN/mm^2, $G_{12} = 4.5$ kN/mm^2 and $v_{12} = 0.36$. These elastic constants are seen

290 to be different to the tabulated properties of $E_1 = 21.3$ kN/mm^2 and $E_2 = 9.6$ kN/mm^2 in the Design

291 Manual from Creative Pultrusions (2016). The Design Manual stiffnesses are for a range of

292   pultruded shape sizes and the larger the size is, the lower can be the volume proportion (and maybe

293   fibre volume fraction) of the unidirectional reinforcement. As a consequence of this fact the

294   tabulated moduli of elasticities are for minimum measured from all the shapes in the series range.

295   Because the published stiffnesses are for the whole 1525 series they are less reliable, and this is the

296   engineering reason why the micromechanical modelling laminae stiffnesses in Table 2 are input

297   data for the FE analyses. The web material consists of alternative reinforcing layer of UD and the

298   TSFM having a balanced lay-up, comprising TSFM1 layer at 1.38 mm thickness, UD1 at 1.93 mm,

299   TSFM2 at 1.42 mm, TSFM3 at 1.39 mm, UD2 at 2.01 mm and TSFM4 at 1.47 mm. Note that mid-

300   thickness layers TSFM2 and TSFM3 do not have UD reinforcement between them. Accounting for

301   experimental errors in the resin burn-off testing the thickness of the four TSFM layer can be taken

302   to be constant at 1.4 mm. The UD layers have a nominal constant thickness of 2.0 mm.

303   The strengths listed in the middle column in Table 2 are for the laminate. PFRP materials

304   having the individual fibre reinforcement types (and the same matrix) are not pultruded and so their

305   strength (and stiffness) properties cannot be measured. Matharu (2104) conducted a series of

306   tension and compression coupon tests (in batches of 10) to determine the panel's in-plane strengths.

307   The longitudinal (compression) strength ($f_{1,C}$) for the batch ranges from 280 to 328 N/mm^2, whereas

308    $f_{2,C}$ is found to range from 99 to 153 N/mm^2. The mean longitudinal strength in tension ($f_{1,T}$) at 294

309   N/mm^2 is 4% lower than the mean compression, whereas the transverse tensile strength ($f_{2,T}$) is, as

310   expected, much lower, at 63% of the compression mean of 133 N/mm^2. The mean in-plane shear

311   strength $f_{1,s}$ is 91 N/mm^2 was taken from D'Alessandro (2009). In the FE work the transverse shear

312   strength ($f_{2,s}$) is taken to be $f_{1,s}$.

313   Each (continuum) damage evolution law includes a corresponding fracture energy (or fracture

314   toughness), G_c, that governs crack growth for the modes illustrated in Fig. 1. Fracture energy is

315   defined as the work needed to create a unit area of a fully developed crack. Guidelines for the

316   evaluation of these fracture properties can be found in Pinho *et al*. (2006) and Maimi *et al*. (2007).

317   The four values adopted in this study are listed in the last column in Table 2. They were not

318   experimentally determined, but estimated based on research expertise and data available from the

319   literature (Kelly and Zweben 2000; Girão Coelho *et al*. 2015).

320   The assumed modelling inputs for interfacial mechanical properties are summarized in Table 3.

321   To establish the peak strengths f_I and $f_{II} = f_{III}$ for Eq. (1), in the absence of experimental

322   measurements, the in-plane strengths $f_{2,T}$ and $f_{1,S} = f_{2,S}$ were factored down by adopting a

323   weakening factor f_w, according to guidance from the failure criterion work by Puck and Schürmann

324   (2002), see Knops (2008), and from the computational modelling work by Wimmer *et al*. (2009).

325   The critical normal interface traction (for opening mode) of the cohesive zone elements is therefore

326   assumed to be equal to the transverse tensile strength, $f_{2,T}$, times the weakening factor. The critical

327   shear interface tractions (for sliding and tearing modes) are both assumed to be equal to the shear

328   strength, $f_{2,S}$, times the same weakening factor.

329   It was found in a sensitivity analysis from a series of FE simulations that the overall response

330   for $f_w = 0.25$ gives the one closest to the pin-bearing experimental results from Matharu (2014).

331   With $f_I = 21$ N/mm^2 and $f_{II} = f_{III} = 23$ N/mm^2 the analysis indicates a relatively weak interface

332   between the laminae, as defined by the FE modelling data given in Fig. 2 and Table 2. A similar f_w

333   has already been proposed by Girão Coelho *et al*. (2016) for this same pultruded material when

334   analysing the different structural engineering problem of delamination failure in a pultruded leg-

335   angle shape subjected to tying force, as would be found in a web clip connection between beam and

336   column members.

337   The piecewise linear traction-separation law of the cohesive elements is described according to

338   the lamina strength presented in the last column in Table 2. Using the guidance from Camanho *et*

339   *al*. (2003) the elastic stiffnesses (per unit area) of the interface (K_I, K_{II} and K_{III} associated with f_I, f_{II}

340   and f_{III}) are assumed to be equal to 10^6 N/mm^3. For modes I, II and III illustrated in Fig. 1 the

341   critical energy release rates of $G_{I,c}$ and $G_{II,c} = G_{III,c}$, were taken as 0.2 (200) and 0.5 (500) N/mm

342   (J/m^2), respectively (Girão Coelho 2016).

343

344

Description of the Model

346   Defined in Fig. 2 are the dimensions for the pin-bearing specimen that is to be modelled and

347   analysed. Each plate of 9.6 mm thickness (t) is 80 mm long (e_1) and 80 mm wide (w). The pin

348   diameter (d) is set equal to 11.8 mm for M12 and to 19.8 mm for M20 steel bolting, while the hole

349   diameter (d_0) was taken 2.4 mm larger, based on practical dimensions. This allowed for the

350   maximum clearance hole tolerance size (Anonymous 2012) and the shaft diameter to be identical to

351   the bolt diameter specification. The pin was placed centrally in the hole, which itself is mid-

352   positioned in the top surface. The UD layers are oriented with the fibres aligned to the direction of

353   the bearing load.

354   The FE model is constructed from stacked continuum shell elements with the individual UD

355   and TSFM layers being modelled separately. Although the element SC8R possesses the geometry

356   of a brick, its kinematic and constitutive behaviour is similar to those of conventional shell elements

357   (Abaqus 2016). The continuum shell elements are able to reproduce reliable results in simulations

358   of thin-walled laminated structures by means of only one element in a lamina thickness, owing to a

359   higher-order displacement field (Parisch 1995; Remmers *et al*. 2003). Cohesive interface elements

360   are used to connect together an TSFM and an UD layer to allow for (multi-)delamination failures to

361   occur. As shown in the diagram in Fig. 2 four cohesive interfaces I1 to I4 are modelled. Justification

362   for no cohesive interface between the two touching TSFM layers at mid-thickness is that Matharu

363   (2014) did not observe, after tests, delamination failure over this interface.

364   The in-plane mesh geometry for the interfaces had to be the same as that for the laminae. A

365   typical mesh with its very refined mesh specification is illustrated in Fig. 3, where adjacent to the

366   hole a finer mesh is used to correctly capture delamination and the important contact situation. Note

367   that using mirror symmetry about the two TSFM layers at mid-thickness the mesh is for a thickness

368   of 4.8 mm (or $t/2$). The thickness of interface layers I1 and I2 are $10^{-3}t_{lay}$, based on the 1.4 mm

369   TSFM layer thickness. Element size was increased towards the plate edges to reduce calculation

370 time. The FE mesh specification in our study of the original material has a total of 27834 (M12)

371 continuum shell SC8R elements (or 32520 elements for the M20 specimen), and 18556 COH3D8

372 cohesive elements (M12 and two interfaces) (or 21680 elements for M20 specimen and two

373 interfaces). Interfaces I1 and I2 (or I3 and I4) are included in the FE model.

374   As mentioned earlier the (steel, smooth shafted) pin is modelled as a three-dimensional

375 analytical rigid body revolved shell.

376   Loading of the specimen is simulated by displacing the bottom edge against the fixed pin as

377 indicated by the 'load' arrows in Fig. 2. Vertical deformation is resisted by the contact surface for

378 pin and hole perimeter at the top of the specimen. Contact behavior is modelled with the 'hard'

379 surface-to-surface contact formulation in the normal direction and the friction is modelled using an

380 isotropic friction model with a coefficient of 0.25. Note that the coefficient of friction was not

381 measured (Mottram 2005) for the steel-FRP contact in the through-thickness direction. This

382 represent one of several modelling data assumptions made to complete a successful FE simulation

383 and they have been reported in this paper.

384   The Abaqus implicit analysis is run with the laminae properties listed in Tables 2 assigned to

385 the appropriate UD or TSFM layers and with the interfacial properties in Table 3. For each lamina

386 the Hashin failure criterion (Hashin 1983) is used to predict damage onset (Girão Coelho 2016), and

387 because interfacial delamination failure always occurs first this criterion is of secondary

388 importance. To account for damage progression after crack initiation there is a fracture energy

389 calculated for each of four failure modes using the fracture energies in Table 2 (Girão Coelho *et al*.

390 2015). To assist with numerical convergence of the Abaqus solver the authors used previous

391 simulation ouputs (Girão Coelho *et al*. 2015) to set a global stabilization factor to 2×10^{-4}.

392

393

394 ***Modelling Strategy Validation***

395   Results from static analyses are compared with maximum pin-bearing loads from experiments.

396   In the series of tests a specimen's stiffness was not measured because it had no meaning to the aim

397   of the strength investigations in Matharu's PhD work (2014), which were to establish characteristic

398   values for pin-bearing strengths. In this paper the web material studied by Matharu is referred to as

399   the original (non-aged) material.

400   One finding from the FE simulations is that delamination failure always governs the magnitude

401   of the load for pin-bearing strength and this matches experimental observations. As a direct

402   consequence the relevant Hashin parameters were found to be always below 1.0. This shows that it

403   has been acceptable for the authors to have made the approximate assumption that the laminate

404   strengths in Table 2 could be taken to be the individual laminae strengths. The pin-bearing strength,

405   here expressed in terms of applied load, is reached when there is extensive delamination growth at

406   the two interfaces (I1 and I2), and there is a sudden load drop-off during the displacement

407   controlled loading. Fig. 4 is for plots constructed from Abaqus outputs of load (kN) versus the axial

408   displacement (mm) in the bearing force direction. The grey shaded circle symbols are for numerical

409   results with the larger black filled circle at the load when initiation of delamination fracturing is

410   numerically predicted. In the legend there is (I1) to identify that the critical delamination is at

411   Interface 1, its location is defined in Fig. 2. The batch test results from Matharu (2104) are reported

412   by three representative loads. The batch mean is given by the solid horizontal line, and the

413   maximum and minimum specimen loads are given by the upper and lower dashed lines. The load

414   range between the two dashed lines gives the measured variation from testing a batch of 10

415   nominally identical specimens. The coefficient of variation for the pin-bearing strength (Matharu

416   2014) for the M12 batch is 10.4 and for the M20 batch is 8.8%.

417   Fig. 4(a) is for the M12 pin, and using the same axis scales the equivalent computational results

418   for the M20 pin are reported in Fig. 4(b). The predicted load-displacement response is seen to start

419   off linear, and progress with non-linearity above 15 kN for M12 and 22 kN for M20. The

420   computational response is seen to differ from the virtually linear load-stroke relationship recorded

by the testing machine. Above the loading (defined by filled circle symbol) for delamination

initiation there is a reduction in structural stiffness and the load-displacement response softens with

progressive delamination growth, before ultimate failure. Stiffness degradation after delamination

initiation and progressive growth is not an outcome in testing since delamination onset is believed

to occur at the same instance the peak load is reached. Importantly, should the FE modelling

methodology presented herein be used to aid the design of bolted connections the predicted load for

delamination initiation is useful because as Figs. 4(a) and 4(b) show it is below the lower bound test

result.

Returning to the information in Fig. 4, the peak (Abaqus) loads of 23 kN (Fig. 4(a) for M12)

and of 35 kN (Fig. 4(b) for M20) compare favourably with the mean experimental loads (Matharu

2014) of 22 kN and 34 kN, respectively. The predictions are in very good agreement with computed

strengths only 4.5% and 6% higher. The positive correlation shown by the results in Figs. 4(a) and

4(b) for two independent batches provides good validation for applying the FE modelling approach

to determine pin-bearing strengths.

In Fig. 5 the deformed shape is shown at peak load (magnification factor is 2.5). Fig. 5(a) is for

the M12 pin and the maximum load of 23 kN, whereas Fig. 5(b) is for the M12 pin at maximum

load of 36 kN. In both parts the deformations clearly shows the typical 'brooming' for compression

induced delamination failure at interfaces I1 (nearest) and I2 (farthest).

Inspection of the localised through-thickness deformation in Fig. 5 helps to explain why

delamination failure is the mechanism that governs the pin-bearing strength. Under the increasing

pressure from the bearing (rigid) pin the existence of Poisson's ratio effect is for the laminate to

need to expand freely in the through-thickness direction. This physically cannot happen because of

the friction restraint over the steel pin/FRP contact area and the volume of the surrounding FRP

material resisting the bearing load. As seen in Figs. 5(a) and 5(b) the deformation is in the form of a

bulge with a short wavelength ($\cong 0.44d_0$). A complex, through-thickness stress field with tension (in

the z-direction) is generated local to the hole perimeter, and within the influence of the bulge zone.

447 It can be speculated that when the maximum through-thickness tensile stress reaches f_I, or the limit

448 given by Eq. (1) when f_I interacts with f_{II} and f_{III} there will be cohesive failure for initiation of

449 delamination failure. Propagation of a delamination crack to the final size shown, for example, in

450 Fig. 6 is numerically controlled by fracture mechanics (Girão Coelho 2016) and the energies listed

451 in Table 3.

452   The contour plots presented on interface surfaces in Fig. 6 show that, at maximum load,

453 delamination fracturing at the two interfaces has progressed from the hole into the body of the

454 specimen. Fig. 6 parts (a) and (b) are for the M12 and M20 bolt diameters, respectively. Damage

455 progression can be tracked, from 0 (none) to 1 (complete), using the Abaqus output parameter

456 Stiffness DEGradation (SDEG), which indicates the state of damage in the cohesive elements and

457 thereby provides insight into damage initiation and propagation. The red coloured area (SDEG is

458 0.7 to 1.0) is for complete interface separation and the thin (green coloured) zone around the

459 damage zone's perimeter is for partial damage (SDEG is 0.3 to 0.7). Where the material on the

460 interface surface is coloured dark blue there is no damage (for SDEG < 0.3), with full continuity

461 across the interface. Interface I1 is on the left-side and interface I2 on the right-side. One

462 observation from the contouring presented in Fig. 6 is that the delamination damage has progressed

463 from an initial state with a stable crack front; this is evidence for bearing failure offering the bolted

464 connection a level of damage tolerance.

465   Overall, we find that the predicted delamination cracks are fairly repeatable and overall are

466 representing the visual observations of bearing surface cracking made by Matharu (2014). The

467 numerical results presented in Figs. 4 to 6 demonstrate the ability of the FE modelling methodology

468 to appropriately predict the pin-bearing mode of failure where interaction between intralaminar and

469 interlaminar modes is strongly coupled.

470

471

Changing the Bearing Strength for Bolted Connections

It is well-known that by increasing the size of the clearance hole the bearing strength decreases (Yuan *et al*. 1996). Figs. 7 and 8 are equivalent to Figs. 4 and 6. In Fig. 7 there are two further load-displacement results for clearance holes of 0 mm (tight fitting) and 1.6 mm (without fabrication tolerance (Anonymous 2012)). Although there is a gain in delamination initiation and maximum loads on reducing clearance from 2.6 to 1.6 mm, there is a significant increase in their values, at 48% (M12) and 39% (M20), for the no clearance situation. Even the change in load on having the clearance equal to the nominal design guideline of 1.6 mm (Creative Pultrusions 2016; Strongwell 2016) justifies why testing for the characteristic strength (Mottram and Zafari 2011; Matharu 2014) has to be with the maximum practical clearance. Illustrated in Fig. 8 are the delamination zones for no clearance and the maximum loads of 25 kN for M12 (Fig. 8(a)) and of 37 kN for M20 (Fig. 8(b)). By inspection it can be seen that the shape of the delamination cracks at interfaces I1 and I2 are broadly similar to those in Figs. 6(a) and 6(b) when the clearance hole is 2.6 mm. Because the tight fitting situation generates pressure over the whole semi-circular notch there is interfacial failure in the laminate beyond the boundary of the hole. This finding shows that the test method applied by Matharu (2014) will not give the actual pin-bearing strength if it is practical on- or off-site to assemble a bolted lap-joint with no hole clearance. By applying our FE modelling approach it is feasible to establish the clearance size at which the delamination growth at peak load first goes beyond the confines of the bolt hole perimeter.

Keeping all other parameters constant to those in Matharu's testing, the next change to be evaluated by a sensitivity analysis is the relative thicknesses of the UD and TSFM layers (for a constant specimen thickness (t) of 9.6 mm). For both bolt diameters Table 4 reports the numerical results of: elastic stiffness (S_{el}); pin-bearing load for initiation of delamination ($R_{br,ID}$); maximum pin-bearing load ($R_{br,max}$); the two load ratios of $R_{br,ID}/R_{br,max}$ and $R_{br,max}/R_{br,max,baseline}$, where $R_{br,max,baseline}$ is the maximum pin-bearing load for the original material (i.e. 23 and 36 kN for M12 and M20, respectively). The original material's predictions are presented in the first row of

498   numbers, with three parametric variations given in the next three rows. The percentage of TSTM in

499   t is 58% in the original material and ranges from 42 to 67% in the three sensitivity analysis

500   materials. As expected, S_{el} increases as the UD percentage increases. Combining the M12 and M20

501   pin results it is found that neither $R_{br,ID}$ nor $R_{br,max}$ show any definite trends. $R_{br,max}$ is seen to remain

502   virtually constant at 23-24 kN (M12) or 35-36 kN (M20). These observations are highlighted by the

503   virtually constant load ratios for the two bolt sizes.

504   The next study investigates the effect of changing the thickness of the mid-thickness TSFM.

505   One reason for this parametric study is that the maximum load is governed by delamination failure

506   at interface I1, not I2 that is for the outer interfaces of the mid-thickness mat layer. The presentation

507   of information and computed predictions in Table 5 is the same as in Table 4. The parameter change

508   is given in the second column where the thickness of the mid-thickness TSFM reduces in four

509   increments to $0t_{orig}$ from its original specification of 2.8 mm ($1.0t_{orig}$). The loss in the thickness of

510   the middle TSFM is replaced by UD reinforcement, shared equally by the two equal-thickness UD

511   layers. One observation is that the material with $0t_{orig}$ and the M12 pin has the highest $R_{br,ID}$ at 21

512   kN. With the M20 bolt size the highest $R_{br,ID}$ of 33 kN is for $0.15t_{orig}$. There is, again, not a

513   significant change in $R_{br,max}$ with the parametric variation, which for M12 is either 23 or 25 kN, and

514   for M20 is 36, 37 or 38 kN.

515   Note that the delamination contours for the specimens covered in Tables 4 and 5 were found to

516   be similar to those shown in Fig. 6. They are not reported in this paper because of lack of space.

517   Returning to the original study parameters (Matharu 2014), the next variable to be examined is

518   reversing, in the laminate, the stacking sequence of layer TSFM1 or layer TSFM2 or of both. In the

519   original material interfaces I1 and I2 had UD fibres on one side and +45° fibres from TSFM on the

520   other side. By reversing the TSFM layer the interface has UD and chopped strand fibres in contact.

521   Information in Table 6 follows Tables 4 and 5 with the stacking sequence changes given in the

522   second column. The results are difficult to interpret with little change in predictions with the M12

523   pin and a significant increase to 1.16 in ratio $R_{br,max}/R_{br,max,baseline}$ when the larger M20 pin is

524   employed.

525   In the 1990s the wide flange shapes (Mottram and Zafari 2011) from Creative Pultrusions Inc.

526   (2016) did not have a triaxial mat reinforcement. Prior to introducing the Pultrex® SuperStructurals

527   product range the mat reinforcement was an CSM, having a local glass fibre volume fraction of

528    $\cong$23%. For the next study the material has either TSFM or CSM for the mat reinforcement. For

529   these simulations the model did not have the mid-thickness mat reinforcement. Predictions are

530   presented in Figs. 9 and 10 in the usual way. In the plots in Fig. 9 the load-displacement response

531   for the original laminate (Matharu 2014) is given by the shaded filled circle symbols. Superimposed

532   on this curve are the predicted results when the TSFM is fully replaced with CSM. The higher pair

533   of curves in Figs. 9(a) and 9(b) is for the situation where the mid-thickness mat is replaced by UD

534   reinforcement, thereby increasing S_{el}. A difference observed is that the maximum load is slightly

535   higher with the 'older' mat reinforcement and it occurs at a higher axial displacement. The positions

536   of the open unfilled circle for the load at delamination initiation show that another difference on

537   having CSM reinforcement is that failure is delayed by about 2 kN (M12) or 4 kN (M20). A key

538   finding is that the maximum loads are the same at 25 kN (M12) and only slightly different at 38 and

539   40 kN (M20) after replacing the TSFM with CSM. An important conclusion from this study is that

540   the presence of ±45º fibres in the TSFM layers has not increased the pin-bearing strength.

541   What is observed from looking at the contour plots in Figs. 10(a) and 10(b) for delamination

542   growth at maximum load is that the shape of the fractured zone is much more centrally located and

543   goes further into the specimen when the mat reinforcement is CSM. The area associated with

544   partially damaged material is seen to be larger too. These figures show that the size and shape of a

545   delamination crack will depend on the orientations of the fibres in the two layers adjacent to the

546   failed interface.

547   The final two FE simulations were performed to find out if pin-bearing strength increases when

548   the chopped strand backing in the TSFM layer is replaced by proportional increases in the 90º and

±45° fibre reinforcements. The rationale for this parametric study is that the chopped strand layer

has a relatively low fibre volume fraction at 16% and occupies 39% of the TSFM's 1.4 mm

thickness. The predicted results are reported in Figs. 11 and 12. As observed from the two curves in

Fig.11 there is little difference in the response up to when delamination failure initiates. Perhaps,

unexpected it is found that the original TSFM with the chopped strand backing has the higher

maximum load for both M12 (i.e. 23 and 18 kN) and M20 pins (i.e. 35 and 29 kN). Comparing the

equivalent contour plots in Fig. 12 with those presented in Fig. 6 it is seen that shape and size is

dependent on the fibre reinforcement local to the failing interface.

Results for this, and other parametric studies reported in this paper have shown that pin-bearing

strength can be highest when the mat reinforcement has random continuous or chopped fibres at the

relatively low volume fraction of < 25%.

Concluding Remarks

A FE modelling methodology using Abaqus software, without customized user-subroutines, has

been formulated that can be employed in parametric and/or sensitivity analyses to determine the

pin-bearing strength of laminated composite materials. Numerical outputs are able to predict the

initiation and growth of delamination failures that governs what a pin-bearing strength is. Using

batch test results for a 9.6 mm thick web from a pultruded structural shape the simulation results for

the two pin diameters of 12 and 20 mm are shown to give good strength predictions. To assist

designers of bolted connections an interesting finding is that initiation of delamination cracking is

not at the peak load, and that this predicted load is close to, yet below the lowest pin-bearing

strength measured from a batch of 10 specimens. There was, however, no observable evidence that

there was stable delamination failure(s) during testing before the pin-bearing strength load was

reached. Although this finding shows that the computational solution differs from the actual pin-

575 bearing response an important finding is that the FE modelling methodology can reliably establish

576 the ultimate failure load for pin-bearing failure.

577 To demonstrate the potential of applying the modelling approach to investigate how the pin-

578 bearing strength might vary with parameter changes a number of parametric studies are presented.

579 While maintaining constant the other parameters in the test series, numerical predictions are

580 reported for changing the: clearance hole size; relative thickness of the unidirectional and triaxial

581 mat layers; thickness of the mid-thickness triaxial mat layer; stacking sequence of the triaxial mat

582 layer; triaxial mat to a continuous strand mat; triaxial mat's construction so that the 39% thickness

583 of chopped strand backing is replaced proportionally with reinforcement having the orientations of

584 $\pm 45^{\circ}$ and 90°.

585 The main findings from the numerical results can be summarized as follows. New

586 understanding is obtained from contour plots for the Abaqus output Stiffness DEGradation showing

587 the size and shape of delamination failure(s) over interfaces. As expected, pin-bearing strength is

588 found to increase with reduced hole clearance and is significantly higher (at 48% and 39% for the

589 two pin diameters) when there is no clearance. Under the tight fitting condition it is observed that

590 the test method (Matharu 2014) becomes invalid because, at peak load, delamination failure is not

591 contained within the semi-circular hole. A less expected finding is that the strength is not sensitive

592 to the relative thicknesses of the unidirectional and mat layers, and there is no benefit on having

593 replaced the continuous strand mat with a triaxial mat (which is more expensive). Furthermore,

594 tabulated results from parametric studies do not offer obvious trends, and the authors cannot give

595 any scientific explanation to why computed results are seen to be highly dependent on the pin

596 diameter being either 12 or 20 mm. The final study shows that strength is reduced on replacing the

597 chopped strand backing in the triaxial mat layers; the opposite might be expected since the

598 additional $\pm 45^{\circ}$ fibres ought to be effective in resisting a higher bearing load.

599 The satisfactory performance of the computational predictions in determining the response at

600 peak load encourages the authors to recommend that the Abaqus modelling methodology may be

601 used to: (i) design the laminate (produced by the pultrusion composite processing method) for a

602 specified pin-bearing strength; (ii) predict the pin-bearing strengths for bolted connections having

603 parameters to be scoped in a structural design standard.

604

605

References

607

608 Abaqus [Computer Software], "*ABAQUS Unified FEA – Complete solutions for realistic*

609 *simulation*," Version 6.14, Dassault systems,

610 http://www.3ds.com/products-services/simulia/products/abaqus. (last assessed 01/08/2016)

611 Anonymous. (2012). '*Code of standard practice for fabrication and installation of pultruded FRP*

612 *structures*,' ANSI standard, American Composites Manufacturers Association, 1st Edition,

613 Arlington, VA..

614 Anonymous. (2016). "*Fiberglass pedestrian and trail bridges*, E. T. Techtonics, Alum Bank, PA,

615 USA. http://www.ettechtonics.com/ (accessed 01/08/2016)

616 ASTM (American Society for Testing and Materials). (2011). "Standard test method for ignition

617 loss of cured reinforced resins." *D*2584-11, West Conshohocken, Pennsylvania, U.S.A.

618 Bank, L. C. (2006). *Composites for construction: Structural design with FRP materials*, John Wiley

619 & Sons, New Jersey, U.S.A.

620 Benzeggagh, M. L, and Kenane, M. (1996). "Measurement of mixed-mode delamination fracture

621 toughness of unidirectional glass/epoxy composites with mixed-mode bending apparatus."

622 *Compos. Sci. Technol.*, 56, 439–449.

623 Brewer, J. C, and Lagace, P. A. (1988). "Quadratic stress criterion for initiation of delamination." *J.*

624 *Compos. Mater.*, 22, 1141–1155.

625 BS EN 1993-1-1:2005. "*Eurocode 3 - Design of steel structures - Part 1-1: General rules and rules*

626 *for buildings*," British Standards Institution (BSI), London.

627   Camanho, P. P., Dávila, C. G., and Moura, M. F. (2003). "Numerical simulation of mixed-mode

628   progressive delamination in composite materials." *J. Compos. Mater.*, 37(16),1415–1438.

629   Creative Pultrusions. (2016). The New and Improved Pultrex1 Pultrusion Design Manual (Imperial

630   Version, Volume 5 Revision 2). Creative Pultrusions, Inc., Alum Bank, PA, USA.

631   http://www.creativepultrusions.com/index.cfm/products-solutions/fiberglass-standard-structural-

632   profiles/pultexc2ae-pultrusion-design-manual/ (accessed 01/08/2016)

633   Chen, Y., Xia, Z., and Ellyin, F. (2001). "Evolution of residual stresses induced during curing

634   processing using a viscoelastic micromechanical model." *J. Comp. Mater.*, 35(6), 522–542.

635   D'Alessandro, R. G. (2009). "*Characteristic values of mechanical properties of wide-flange*

636   *pultruded FRF beams*," MSc Thesis, University of Wisconsin-Madison, USA.

637   Du, A., Liu, Y., Xin, H. and Zuo, Y. (2016). "Progressive damage analysis of PFRP double-lap

638   bolted joints using explicit finite element method," *Comp. Struct.*, 152, 860–869.

639   Falk, M. L., Needleman, A., and Rice, J. R. (2001). "A critical evaluation of cohesive zone models

640   of dynamic fracture." *J. Phys. IV*, Proc 11(Pr.5), 43–50.

641   Girão Coelho, A. M. (2016). "Finite element guidelines for simulation of delamination dominated

642   failures in composite materials validated by case studies." *Arch. Comput. Method. E.*, 23(2),

643   363–388.

644   Girão Coelho, A. M., and Mottram, J. T. (2015). "A review of the behaviour and analysis of bolted

645   connections and joints in pultruded fibre reinforced polymers." *Mater. Design*, 74, 86–107.

646   Girão Coelho, A. M., Mottram, J. T., and Harries, K. A. (2015). "Finite element guidelines for

647   simulation of fibre-tension dominated failures in composite materials validated by case studies."

648   *Comp. Struct.*, 126, 299-313.

649   Girão Coelho, A. M., Mottram, J. T., and Matharu, N. (2016). "Virtual characterization of

650   delamination failures in pultruded GFRP angles." *Compos. Part B – Eng.*, 90, 212–222.

651   Hancox, N. L. and Mayer, R. M. (1994). "*Design data for reinforced plastics, A guide for engineers*

652   *and designers*," Chapman and Hall, London.

653 Hashin, Z. (1983). "Analysis of composite materials." *J. Appl. Mech.*, 50, 481–505.

654 Kelly, A., and Zweben, C. (eds.). (2000). *Comprehensive composite materials*, *vol.* 2, Elsevier

655   Science.

656 Knops, M. (2008). *Analysis of failure in fiber polymer laminates – the theory of Alfred Puck.*

657   Springer, Germany.

658 Lane, A. (2002). *An experimental investigation of buckling mode interaction in PFRP columns,*

659   PhD thesis, University of Warwick, U.K.

660 Maimí, P., Camanho, P. P., Mayugo, J. A., and Dávila, C. G. (2007). "A continuum damage model

661   for composite laminates, part I: constitutive model." *Mech. Mater.*, 39, 897–908.

662 Matharu, N. S. (2014). *Aspects of bolted connections for fibre reinforced polymer structures,* PhD

663   Thesis, University of Warwick, U.K.

664 Mottram, J. T. and Turvey G. J. (2003). 'Physical test data for the appraisal of design procedures for

665   bolted joints in pultruded FRP structural shapes and systems,' *Prog. Struct. Eng. Mater.,* 5(4),

666   195-222.

667 Mottram, J. T. (2005). "Friction and load transfer in bolted joints of pultruded fibre reinforced

668   polymer section." *Proc., 2nd Int. Conf. on FRP Composites in Civil Engineering*, R. Seracino,

669   ed., Taylor & Francis, Adelaide, Australia, 845–850.

670 Mottram, J. T. and Zafari, B., (2011). "Pin-bearing strengths for design of bolted connections in

671   pultruded structures," *P I Civil Eng-Str B*, 164(5), 291–305.

672 Ortiz, M., and Pandolfi, A. (1999). "Finite-deformation irreversible cohesive elements for three

673   dimensional crack-propagation analysis." *Int. J. Numer. Meth. Eng.*, 44, 1267–1282.

674 Parisch, H. (1995). "A continuum-based shell theory for non-linear applications." *Int. J. Numer.*

675   *Meth. Eng.*, 38, 1855–1833.

676 Pinho, A., Robinson, P., and Iannucci, I. (2006). "Fracture toughness of the tensile and compressive

677   fibre failure modes in laminated composites." *Compos. Sci. Technol.*, 66, 2069–79.

678 Puck, A., and Schürmann, H. (2002). "Failure analysis of FRP laminates by means of physically

679   based phenomenological models." *Compos. Sci. Technol.*, 62, 1633–1662.

680 Reichhold. (2006), "*DION® 31031-00 Medium-high reactivity pultrusion resin*", Product Bulletin,

681   Revision date January 2006.

682 Remmers, J. C., Wells, G. N., de Borst, R. (2003). "A solid-like shell element allowing for arbitrary

683   delaminations." *Int. J. Numer. Meth. Eng.*, 58, 1701–1736.

684 Starr, T. (2000). *Pultrusion for engineers*, Woodhead publishing Ltd., Cambridge, U.K.

685 Strongwell. (2016). Strongwell Design Manual. Strongwell, Bristol, VA, USA. See

686   //www.strongwell.com/ (accessed 01/08/2016).

687 Turon, A., Dávila, C. G., Camanho, P. P., and Costa, J. (2000). "An engineering solution for mesh

688   size effects in the simulation of delamination using cohesive zone models." *Eng. Fract. Mech.*,

689   74, 1665–1682.

690 Turvey, G.J. (2000). "Bolted connections in PFRP structures." *Progress in Structural Engineering*

691   *and Materials* 2(2), 146– 156.

692 Wimmer, G., Schuecker, C., and Pettermann, H.E. (2009). "Numerical simulation of delamination

693   in laminated composite components e a combination of a strength criterion and fracture

694   mechanics. *Compos Part B-Eng* 40,158-165.

695 Yuan, R. L., Liu, C. J. and Daley, T. (1996). "*Study of mechanical connection for GFRP laminated*

696   *structures,*" Proceedings of the 2nd International Conference on Advanced Composite Materials

697   in Bridges and Structures (ACMBS-2), The Canadian Society for Civil Engineers, Montreal,

698   951-958.

699 Ye, B. S., Svenson, A. L., and Bank, L. C. (1995). "Mass and volume fraction properties of

700   pultruded glass fibre-reinforced composites." *Composites*, 26(10), 725–731.

701 Zafari, B. and Mottram, J. T. (2012). "Effect of hot-wet aging on the pin-bearing strength of a

702   pultruded material with polyester matrix," *J. Compos. Constr.*, 16(3), 340-352.

703 Zhang, Y., Xia, Z., and Ellyin, F. (2004). "Evolution and influence of residual stresses/strains of

704 fibre reinforced laminates." *Compos. Sci. Technol.*, 64, 1613–1621.

705

706 **Fig. 1.** Modes of delamination failure: a) Mode I (m = I): opening; b) Mode II (m = II): sliding; c)

707 Mode III (m = III): tearing.

708 **Fig. 2.** Geometry: schematic of plate and pin with applied load and composite lay-up showing

709 locations of four interfaces I1 to I4.

710 **Fig. 3.** Typical plate mesh for the evaluation of the (12 mm) pin-bearing behaviour of a pultruded

711 specimen, with the symmetry plane facing backwards.

712 **Fig. 4.** Load-displacement plots from implementing the FE model, and comparison with

713 experimental data from Matharu (2014): a) M12; b) M20.

714 **Fig. 5.** Specimen deformation at maximum predicted load (plots on deformed structure,

715 magnification factor 2.5): a) M12; b) M20.

716 **Fig. 6.** Delamination at interfaces I1 (left) and I2 (right) at maximum predicted load (contour

717 plotting on deformed mesh): a) M12 at 23kN; b) M20 at 36 kN.

718 **Fig. 7.** Effect of changing the size of the hole clearance: a) M12; b) M20.

719 **Fig. 8.** Delamination at interfaces I1 (left) and I2 (right) at maximum load (plots on deformed

720 structure) when specimen has no clearance hole: a) M12 has maximum load of 25 kN; b) M20 has

721 maximum load of 37 kN.

722 **Fig. 9.** Plots to maximum load having mat reinforcement TSFM replaced with CSM (filled markers

723 – TSFM; unfilled markers – CSM): a) M12; b) M20.

724 **Fig. 10.** Delamination growth at interface I1 at maximum load for mat reinforcement of TSFM

725 (left-side) or of CSM (right-side): a) M12 has maximum load of 25 kN | 25 kN); b) M20 has

726 maximum load of 38 kN | 40 kN)

727 **Fig. 11.** Comparison of original material with a new material when the chopped strand layer in the

728 TSFM is replaced by the continuous fibre reinforcements (filled markers – TSFM; unfilled markers

729 – TSFM without chopped strand layer): a) M12; b) M20.

730 **Fig. 12.** Delamination at interfaces I1 (left) and I2 (right) at maximum load when chopped strand

731 layer in the TSFM is not present (plots on deformed structure): a) M12 has maximum load of 18

732 kN; b) M20 has maximum load of 28 kN

733

734

(a)   (b)   (c)

735   Fig. 1

736

(Fixed) Steel pin (diameter d)

d_0

Pultrusion
direction

$e_1 = 80$ mm

$t = 9.6$ mm

Load

$t = 9.6$ mm

$w = 80$ mm

I1 → TSFM1 — 1.4 mm
UD1 — 2.0 mm
I2 →
TSFM2&3 — 2.8 mm
I3 →
UD2 — 2.0 mm
I4 → TSFM4 — 1.4 mm

737

738   Fig. 2
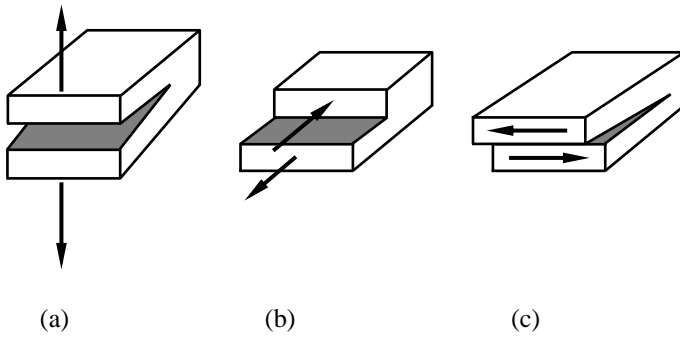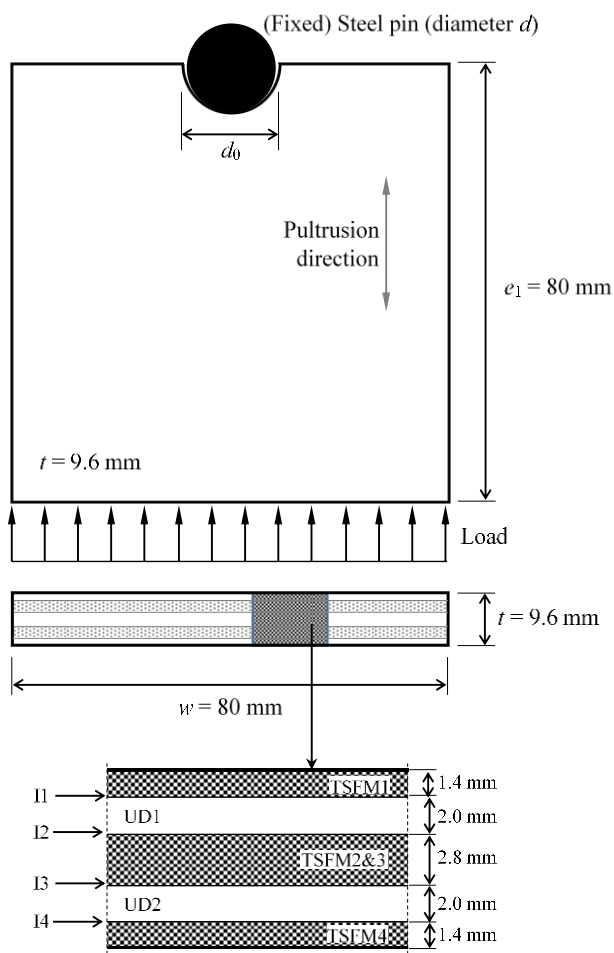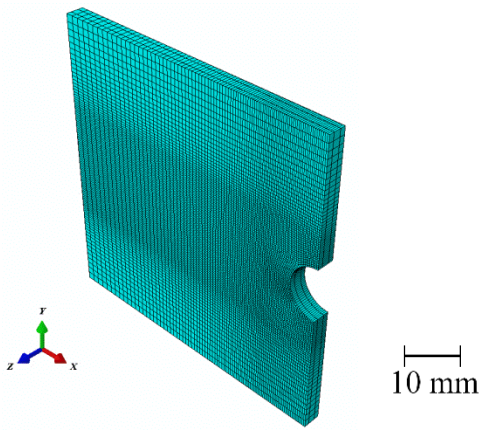
739

740

741   Fig. 3

742
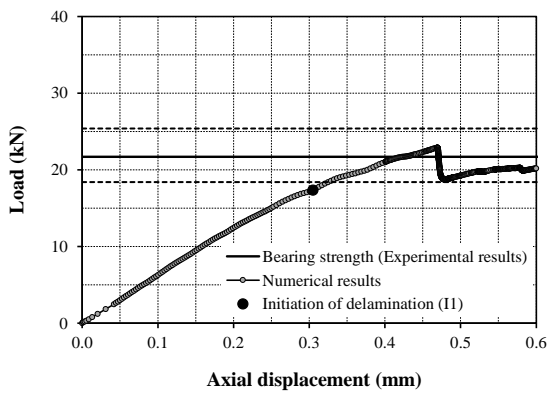
743

744   (a)
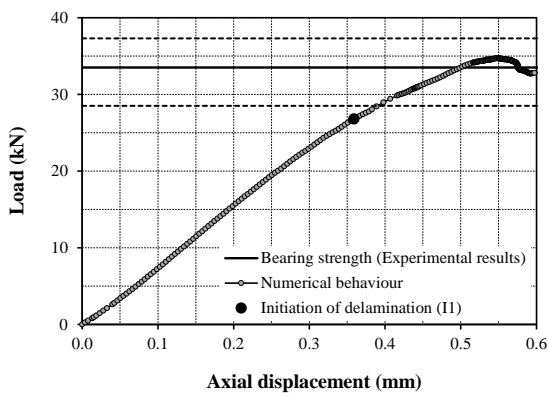
745

746   (b)

747   Fig. 4

748
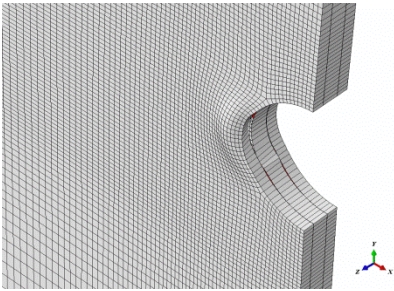
749
750   (a)
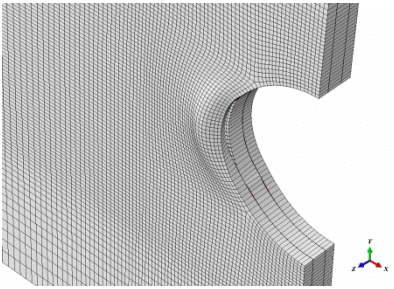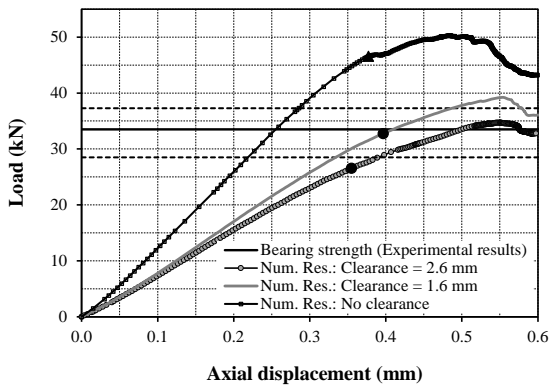

751
752   (b)

753   Fig. 5

754
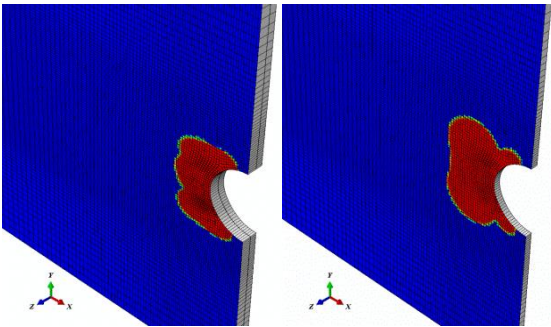
755   (a)
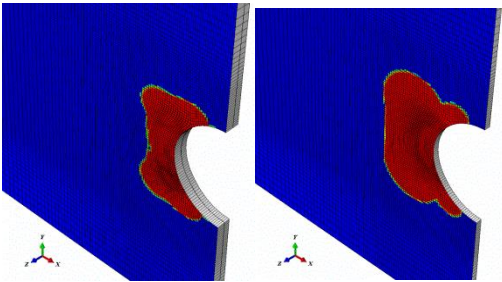
756   (b)

Completely damaged   Partially damaged   Undamaged
(0.7 to 1.0)   (0.3 to 0.7)   less than 0.3
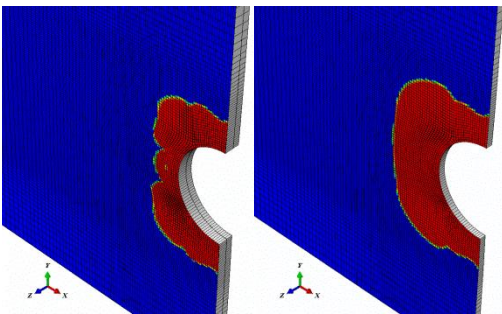
757
758

759   Fig. 6
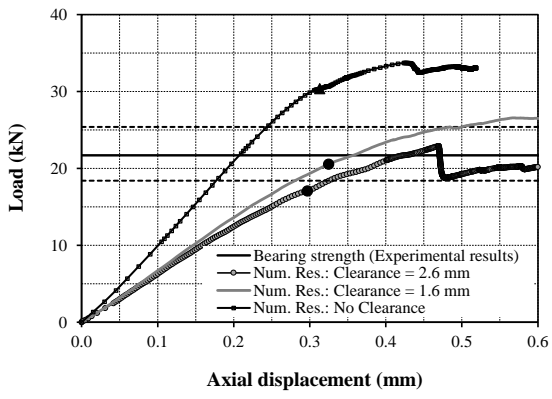
760

761   (a)

762

763   (b)

764   Fig. 7
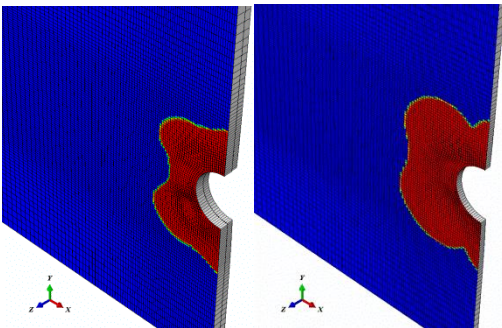
765   (a)

(b)

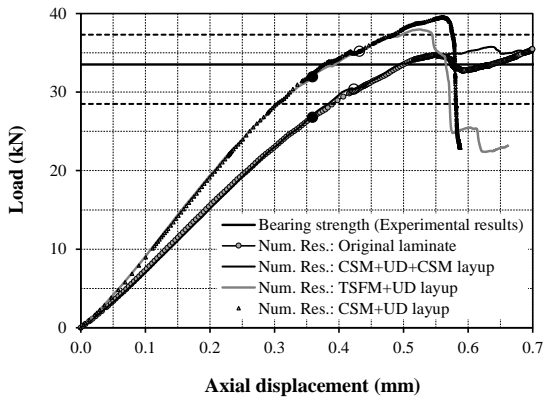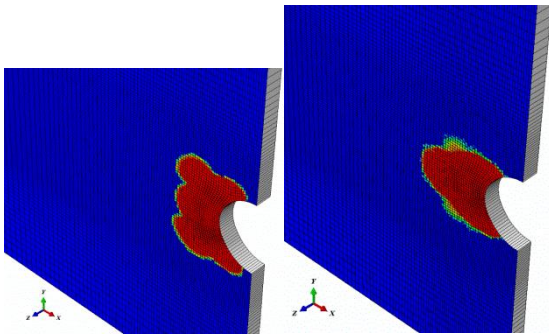| ■ Completely damaged (0.7 to 1.0) | ■ Partially damaged (0.3 to 0.7) | ■ Undamaged less than 0.3 |

766

767   Fig. 8
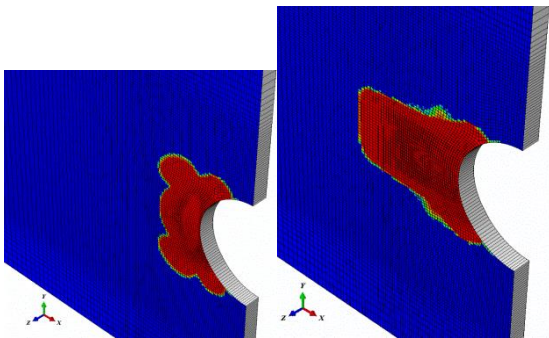
768
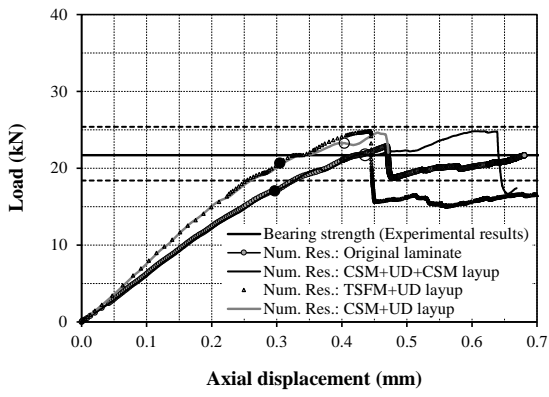
769

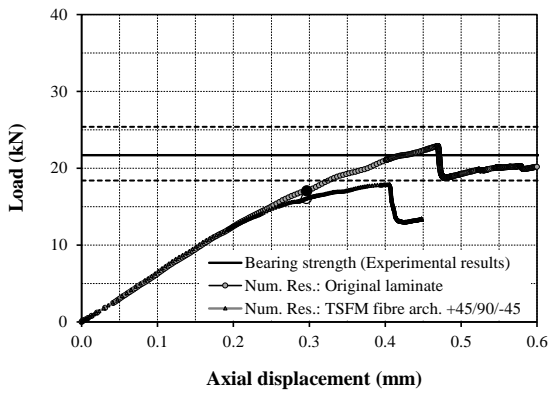770　(a)

771

772　(b)

773　Fig. 9
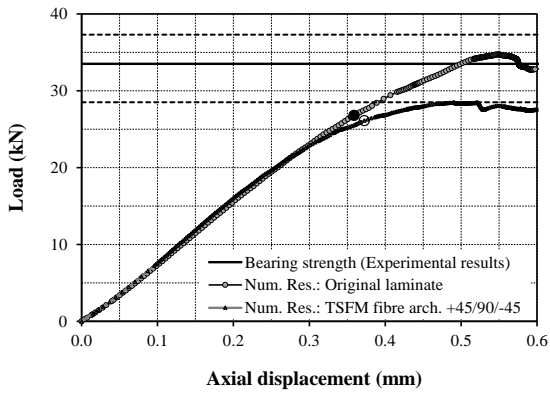

774　(a)

775　(b)

■ Completely damaged (0.7 to 1.0)　　■ Partially damaged (0.3 to 0.7)　　■ Undamaged less than 0.3
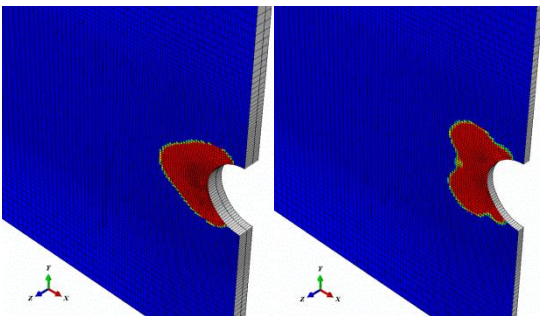
776

777　Fig. 10

778

779 (a)

780

781 (b)

782 Fig. 11

783 (a)
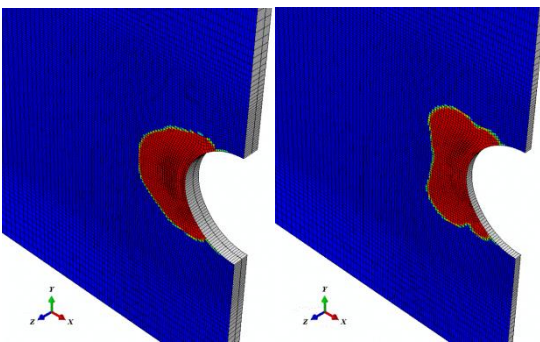
(b)

784

785 Fig. 12

786   **Table 1.** Material constituent properties for the Pultrex® Superstructural material of 9.6 mm

787   thickness.

	Constituent part			
	SV	TSFM	UD	Matrix
Number of layers in thickness	2	4	2	–
Fibre architecture	Random fibre veil	+45°/90°/–45°/CSM	156 (56 yield)	–
% volume fraction	3	34	33	30
% total of fibre reinforcement	5	48	47	–
Nominal layer thickness, t_{lay} (mm)	0.03	1.4	2.0	–

788

789

790

791

792 **Table 2.** Lamina properties for the laminate defined in Fig. 2.

Elastic lamina properties (kN/mm^2)				Laminate strength properties (N/mm^2)		Fracture energy (N/mm)	
	Constituent part						
	UD	TSFM	CSM				
		Mat layer (+45°/90°/−45°)					
E_1	44.7	13.1	7.7	$f_{1,T}$	294	$G_{1,T,c}$	100
$E_2 = E_3$	14.0	25.5	7.7	$f_{1,C}$	306	$G_{1,C,c}$	100
$G_{12} = G_{13}$	4.1	6.1	2.7	$f_{2,T}$	84	$G_{2,T,c}$	1.2
ν_{12}	0.28	0.41	0.41	$f_{2,C}$	133	$G_{2,C,c}$	5
				$f_{1,s} = f_{2,s}$	91		

793

794

795

796 **Table 3.** Interfacial properties for the pultruded FRP laminate defined in Fig. 2.
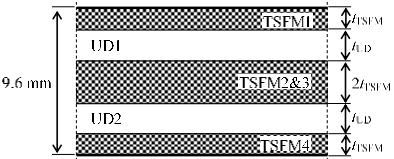
Interfacial properties	
$K_I = K_{II} = K_{III}$ (N/mm^3)	10^6
f_I (N/mm^2)	21[1]
$f_{II} = f_{III}$ (N/mm^2)	23[1]
$G_{I,c}$ (N/mm)	0.2
$G_{II,c} = G_{III,c}$ (N/mm)	0.5

797 Note. These values correspond to a weakening factor of 0.25.

798

799

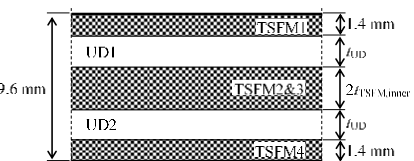800   **Table 4.** Modelling results: relative thickness of layers.

		M12					M20				
		S_{el} (kN/mm)	$R_{br,ID}$ (kN)	$R_{br,max}$ (kN)	$R_{br,ID}/R_{br,max}$	$R_{br,max}/R_{br,max,baseline}$	Sel (kN/mm)	$R_{br,ID}$ (kN)	$R_{br,max}$ (kN)	$R_{br,ID}/R_{br,max}$	$R_{br,max}/R_{br,max,baseline}$
Original material											
t_{TSFM} (mm) (% of t) t_{UD} (mm) (% of t)	1.4 (58) 2.0 (42)	59	17	23	0.75	1.00	82	27	36	0.75	1.00
Parametric variation											
t_{TSFM} (mm) (% of t) t_{UD} (mm) (% of t)	1.0 (42) 2.8 (58)	69	19	23	0.82	1.02	95	31	35	0.89	1.00
t_{TSFM} (mm) (% of t) t_{UD} (mm) (% of t)	1.2 (50) 2.4 (50)	65	15	23	0.63	1.01	74	25	35	0.73	1.00
t_{TSFM} (mm) (% of t) t_{UD} (mm) (% of t)	1.6 (67) 1.6 (33)	58	20	24	0.87	1.05	88	28	35	0.81	1.01

801

802

803 **Table 5.** Modelling results: thickness of internal TSFM layer.

		M12					M20				
		S_{el} (kN/mm)	$R_{br,ID}$ (kN)	$R_{br,max}$ (kN)	$R_{br,ID}/R_{br,max}$	$R_{br,max}/R_{br,max,baseline}$	S_{el} (kN/mm)	$R_{br,ID}$ (kN)	$R_{br,max}$ (kN)	$R_{br,ID}/R_{br,max}$	$R_{br,max}/R_{br,max,baseline}$
Original material											
$t_{TSFM,inner}$ (mm) t_{UD} (mm)	$(1.0t_{orig})$ 1.4 2.0	59	17	23	0.75	1.00	82	27	36	0.75	1.00
Parametric variation											
$t_{TSFM,inner}$ (mm) t_{UD} (mm)	$(0.5t_{orig})$ 0.7 2.7	72	19	23	0.83	0.99	94	30	37	0.82	1.02
$t_{TSFM,inner}$ (mm) t_{UD} (mm)	$(0.25t_{orig})$ 0.35 3.05	77	20	25	0.80	1.11	102	31	37	0.83	1.03
$t_{TSFM,inner}$ (mm) t_{UD} (mm)	$(0.15t_{orig})$ 0.21 3.19	80	17	25	0.68	1.10	99	33	36	0.92	1.01
$t_{TSFM,inner}$ (mm) t_{UD} (mm)	$(0t_{orig})$ 0 3.4	75	21	25	0.83	1.08	105	32	38	0.84	1.06

804

805

806   **Table 6.** Modelling results: stacking sequence TSFM layer.

		M12					M20				
		S_{el} (kN/mm)	$R_{br,ID}$ (kN)	$R_{br,max}$ (kN)	$R_{br,ID}/R_{br,max}$	$R_{br,max}/R_{br,max,baseline}$	S_{el} (kN/mm)	$R_{br,ID}$ (kN)	$R_{br,max}$ (kN)	$R_{br,ID}/R_{br,max}$	$R_{br,max}/R_{br,max,baseline}$
Original material											
$t_{TSFM,1}$	+45°/90°/-45°/CSM	59	17	23	0.75	1.00	82	27	36	0.75	1.00
$t_{TSFM,2}$	+45°/90°/-45°/CSM										
Variation											
$t_{TSFM,1}$	+45°/90°/-45°/CSM	59	19	24	0.77	1.05	82	27	35	0.79	0.96
$t_{TSFM,2}$	CSM /-45°/90°/45°										
$t_{TSFM,1}$	CSM /-45°/90°/45°	59	20	23	0.87	1.01	82	33	37	0.88	1.08
$t_{TSFM,2}$	+45°/90°/-45°/CSM										
$t_{TSFM,1}$	CSM /-45°/90°/45°	59	20	23	0.88	1.01	82	33	40	0.82	1.16
$t_{TSFM,2}$	CSM /-45°/90°/45°										

807

808